# Myocardium Segmentation From DE MRI Using Multicomponent Gaussian Mixture Model and Coupled Level Set

Jie Liu, Xiahai Zhuang, Lianming Wu, Dongaolei An, Jianrong Xu, Terry Peters, *Fellow, IEEE*, and Lixu Gu\*, *Senior Member, IEEE*

*Abstract*—*Objective:* In this paper, we propose a fully automatic framework for myocardium segmentation of delayed-enhancement (DE) MRI images without relying on prior patient-specific information. *Methods:* We employ a multicomponent Gaussian mixture model to deal with the intensity heterogeneity of myocardium caused by the infarcts. To differentiate the myocardium from other tissues with similar intensities, while at the same time maintain spatial continuity, we introduce a coupled level set (CLS) to regularize the posterior probability. The CLS, as a spatial regularization, can be adapted to the image characteristics dynamically. We also introduce an image intensity gradient based term into the CLS, adding an extra force to the posterior probability based framework, to improve the accuracy of myocardium boundary delineation. The prebuilt atlases are propagated to the target image to initialize the framework. *Results:* The proposed method was tested on datasets of 22 clinical cases, and achieved Dice similarity coefficients of $87.43 \pm 5.62\%$ (endocardium), $90.53 \pm 3.20\%$ (epicardium) and $73.58 \pm 5.58\%$ (myocardium), which have outperformed three variants of the classic segmentation methods. *Conclusion:* The results can provide a benchmark for the myocardial segmentation in the literature. *Significance:* DE MRI provides an important tool to assess the viability of myocardium. The accurate segmentation of myocardium, which is a prerequisite for further quantitative analysis of myocardial infarction (MI) region, can provide important support for the diagnosis and treatment management for MI patients.

*Index Terms*—Coupled level set, delayed-enhancement MRI, multi-component Gaussian mixture model, myocardium segmentation.

J. Liu is with the School of Biomedical Engineering, Shanghai Jiao Tong University.

X. Zhuang is with School of Data Science, Fudan University.

L. Wu, D. An, and J. Xu are with Department of Radiology, Renji Hospital, Shanghai Jiao Tong University School of Medicine.

T. Peters is with Robarts Research Institute, University of Western Ontario.

\*L. Gu is with the School of Biomedical Engineering, Shanghai Jiao Tong University, Shanghai 200240, China (e-mail: gulixu@sjtu.edu.cn).

## I. INTRODUCTION

ASSESSMENT of myocardial viability is essential in the diagnosis and treatment management for patients suffering from myocardial infarction (MI). Delayed-enhancement (DE) MRI provides an important tool for MI assessment, because of its capability to directly visualize infarcts, and the established effectiveness in determining the presence, location, and extent of MI. In DE MRI, the infarcted myocardium is enhanced due to the delayed washout of contrast agent compared to the healthy myocardium.

Once the myocardium has been delineated in DE MRI images, the MI regions can be differentiated from healthy tissue using a method based on appropriate intensity threshold. For example, with manually annotated remote healthy tissue as reference, the mean ($\mu$) and standard deviation ($\sigma$) of the intensity of the reference region can be calculated, and the threshold can be determined as $\mu + n \cdot \sigma$, where $n$ is an empirically determined integer [1]–[3]. Alternatively, the full width at half-maximum (FWHM) of the MI region can be employed as a thresholding criterion [1], [3]. Several classification techniques have also been introduced into the segmentation of MI regions, such as the k-means [4], fuzzy c-means [5], [6], mixture model, including the Rayleigh-Gaussian mixture model [7], [8], Gaussian mixture model [5], [9] and Rician-Gaussian mixture model [9]. Fast level set algorithms [10], region competition [7], watershed segmentation [8], [9], and region growing [11], have also been employed to address this problem. However, before the MI can be identified and analyzed quantitatively the myocardium must first be segmented. Currently, this is often performed manually or semi-automatically in clinical practice. Since manual delineation can suffer from intra- and inter-observer variation and be time consuming, the automated segmentation becomes increasingly desired.

Developing fully automated segmentation from cardiac images is generally arduous due to the large shape variability of heart, indistinct boundaries, and the low quality of images due to motion artifacts [12], [13]. In addition, the automatic segmentation from cardiac DE MRI must tackle another three challenges coming from the contrast enhancement:

1) The intensity of the myocardium is heterogeneous due to the existence of the enhanced infarct regions. This challenges many of the automatic myocardium segmentation

methods that can work well in other MRI sequences, such as the cine MRI, where uniformity of the intensity distribution is often assumed [14], [15].

2) The enhancement patterns are complex, with the location and size of infarcts varying markedly across different patients. Microvascular obstruction also occurs in many patients, where part of the infarct regions appears dark due to the lack of contrast agent uptake. It is, therefore, difficult to make any geometric assumption of the infarcts.

3) The intensity range of the myocardium fully overlaps that of its surroundings, e.g. the healthy myocardium has an intensity range similar to that of the liver and lung, and the enhanced myocardial infarct has a similar range to that of the blood pool.

To the best of our knowledge, little work has so far focused on the automatic or semi-automatic segmentation of myocardium from DE MRI. Rajchl *et al.* [16] proposed to extract myocardial infarcts directly in a semi-automated manner, and the healthy myocardium was also segmented implicitly. This method limits the use of the prior knowledge about myocardium (contains the healthy and infarcted regions) to minimize the need for human supervision. Many of the automatic methods use the myocardial segmentation of cine MRI acquired in the same session as *a priori* knowledge, since cine MRI is widely used in clinics. The prior segmentation in cine MRI is first propagated to the DE images using image registration techniques and more accurate segmentation can be obtained by applying an additional global affine transformation [17] or a shift window [18] to the 2D slices. Also a 3D mesh can be built from the propagated prior segmentation and then deformed towards the target myocardial contours. Different models have been proposed, based on the intensity characteristics of DE images and the myocardium shape knowledge, to detect the myocardial contours. Ciofolo *et al.* [19] proposed a 2D geometrical template which modeled the myocardium as a closed ribbon structure with an imaginary centerline and variable width. They divided the myocardium into four quadrants and treated those containing potential scars differently while deforming the 2D template. Wei *et al.* [20] used a 1D profile template to model the intensity patterns along a radial ray from the left ventricle (LV) center to beyond the epicardium. The paired endocardial and epicardial edge points are detected along the radial ray. However, these existing models are not sufficiently flexible to adapt to the complex enhancement patterns in MI patients. The work of [16] and [18] mainly targeted the infarction region and no quantitative evaluation of the myocardium segmentation was provided. Though many automatic segmentation methods from cine MRI have been established, the use of cine MRI as a prior makes the whole segmentation procedure tedious and time consuming. The segmentation errors in cine MRI can be propagated to the segmentation of DE MRI. Also, an accurate registration between the two sequences can be challenging. Therefore, human supervision is often required in several stages.

In this paper, we focus on the fully automatic myocardium segmentation from DE MRI. We explore the possibility of accurately delineating the myocardium from DE MRI without additional prior information of the specific subject, such as b-SSFP

cine MRI. We make full use of the information from a single sequence and reduce the dependence on the initial contours, and thus simplify the whole segmentation procedure. We employ the multi-component Gaussian mixture (MCGM) model [21] to deal with the intensity heterogeneity of myocardium. The traditional Gaussian mixture model (GMM) assumes the intensity of each anatomical structure to be Gaussian distributed, which in many situations cannot be justified. On the other hand, the MCGM models the intensity distribution of a structure, e.g. myocardium, with multiple Gaussian functions, i.e. multiple components. To estimate the model parameters, the expectation maximization (EM) algorithm is employed and an atlas prebuilt from healthy volunteers is propagated to initialize the parameters.

To maintain the spatial continuity and a realistic myocardial shape, a spatial regularization is required. A pre-constructed atlas can be used to propagate constraints to the target image [21], [22]. However, accurate propagation of such constraints via atlases is difficult, and an improper spatial constraint can limit the flexibility of contour evolution, leading to inaccurate segmentation results. To ameliorate this problem, we introduce the coupled level set (CLS) to serve as the spatial regularization, which can be iteratively adapted to the image characteristics while the propagated atlas is usually fixed throughout the segmentation process. The active contour method has been successfully used in image segmentation, and the extension to the multiphase segmentation has also been studied [23], [24]. Zeng *et al.* [25] introduced the idea of coupled-surfaces propagation during cortical segmentation, reflecting its elongated shape and approximately constant thickness. This idea was later extended to myocardial segmentation in short axis images for the coupled propagation of two cardiac contours [26]. Many myocardial segmentation efforts were based on the CLS using different image information, or integrating different prior knowledge [27]. In the work related to bladder wall segmentation, Han *et al.* [28] introduced the CLS into the EM framework, where the level set energy function was constructed based on the posterior probability updated in the EM iteration. Inspired by these works, the CLS and EM frameworks are adopted in our myocardium segmentation. We introduce the CLS as a shape regularization step. The CLS evolution is not only based on the posterior probability estimated in the EM estimation step, but also on the intensity gradient information computed from the target image.

The rest of the paper is organized as follows: the proposed method is described in Section II; the experiments and results are presented in Section III; conclusions are given in Section IV.

## II. METHOD

This work attempts to classify pixels of DE MRI images into three spatially coherent classes: the myocardium, LV and background. First, an atlas is registered to the target image [29], [30], to initialize the prior class probabilities for each image pixel. Image intensity distribution of the three class are modeled by MCGM model (described in Section II-A), and the model parameters are estimated using the EM algorithm (described in Section II-B). The MCGM model only accounts for the intensity information, and all the pixels are assumed to be mutually independent. We therefore introduce a CLS to impose

MCEM-CLS framework
Register atlas to target
Initialize the mean and variance, mixture proportions using (8-11)
While not converged of posterior probability
E-step: calculate posterior probability using (4)
M-step: update the mean and variance, and mixture proportion using (5-7)
Evolve CLS using (16-17)
Update the prior probability using (20)
End of While
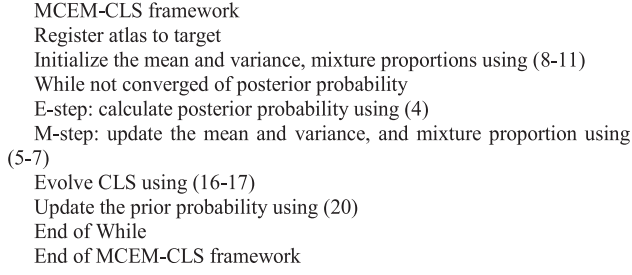End of MCEM-CLS framework

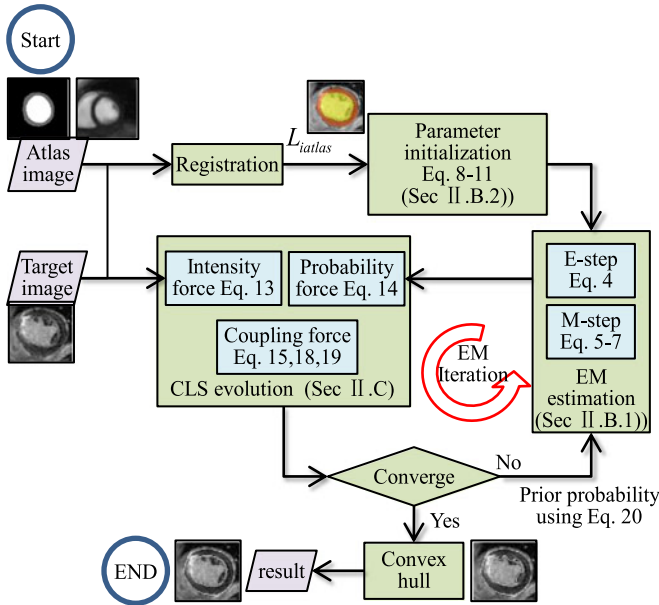Fig. 1.    Pseudo code of the proposed MCEM-CLS framework.



Fig. 2.    Flowchart of the proposed myocardium segmentation for cardiac DE-MRI.
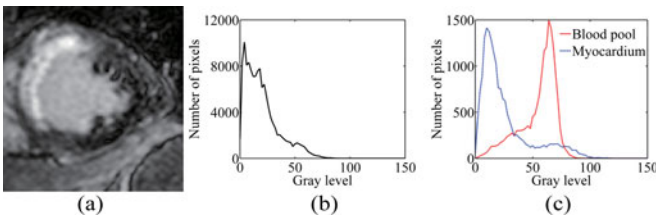


Fig. 3.    DE MRI images and corresponding intensity distribution. (a) one example of DE MRI slice; (b) the intensity histogram of the image in (a); (c) the intensity histogram of myocardium and blood pool.

a spatial regularization on the prior probabilities (described in Section II-C). In the CLS, two contours, respectively representing the epicardial and endocardial surfaces, are evolved to fit the image under the influence of the coupling force, the posterior probability force, and the image intensity force. The CLS regularization step takes place after the posterior class probability is re-calculated with the updated MCGM parameters, and then forms the new prior probabilities to trigger a new iteration. Fig. 1 provides the pseudo code of the proposed segmentation framework, and Fig. 2 illustrates the flowchart.

## A.  Multi-Component Gaussian Mixture Model

The GMM method assumes that each target class should have a unique intensity with added noise that can be modeled by a Gaussian distribution. However, in the context of medical imaging, the images and target objects usually do not follow such a simple assumption, and there is no simple one-to-one correspondence between the target classes and the Gaussian distributions. In the segmentation task described in this paper, one class can indeed be modeled by a combination of several Gaussian distributions. For example, the myocardium contains healthy tissue as well as enhanced infarcts. Similarly, pixels from different classes may have similar intensities: the intensity of infarcts and blood pool can be very similar, and it is difficult to differentiate them based merely on intensity. From the perspective of target classes, one can adopt the MCGM model [21], which allows one target class to contain multiple components of Gaussian distributions. To correctly classify the pixels with similar intensities into different target classes, we introduce the spatially variant class prior probabilities and impose myocardium spatial information using the CLS which is described in detail in Section II-C.

With the MCGM model, we classify all the pixels into three classes, $\Lambda = \{L_{\mathrm{LV}}, L_{\mathrm{myo}}, L_{\mathrm{bg}}\}$, namely the LV, myocardium and background. The LV class contains one component; the myocardium contains two components, respectively for the healthy and infarcted tissues; the background contains three components: lung, liver and right ventricle (RV). We denote the set of all the components as $X$. The intensity distribution of each component is modeled as a Gaussian distribution. Let $l_i$ and $z_i$ ($i = 1, 2, \ldots, N$, where $N$ is the total number of pixels) denote the class and the component to which pixel $i$ belongs, respectively. With the assumption that the observed intensity $y_i$ is independent of $l_i$ conditionally to $z_i$, the MCGM model can be written as follows:

$$f\left(y_i | \mathbf{\Phi}, \mathbf{\Pi}\right) = \sum_{L \in \Lambda} p\left(l_i = L\right) \sum_{C \in X} p(z_i = C | l_i$$
$$= L)\phi\left(y_i | \mu_C, \sigma_C\right), \qquad (1)$$

where $\phi(y_i | \mu_C, \sigma_C)$ is the Gaussian distribution with mean $\mu_C$ and standard variance $\sigma_C$; $p(l_i = L)$ is the prior probability of pixel $i$ belonging to the class L, which varies from pixel to pixel. For simplicity, we denote $\phi_{iC} = \phi(y_i | \mu_C, \sigma_C)$ and $\pi_{iL} = p(l_i = L)$. We denote $p_{iC} = p(z_i = C | y_i)$ as the posterior probability of pixel $i$ belonging to component $C$ and $p_{iL} = \sum_{C \in L} p_{iC}$ as the posterior probability of pixel $i$ belonging to class L. In the case that pixel $i$ belongs to class L, the mixture proportion of the component $C \in L$ is represented by $\delta_{LC}$, i.e.

$$p\left(z_i = C | l_i = L\right) = \begin{cases} \delta_{LC}, & C \in L \\ 0, & C \notin L \end{cases}, \qquad (2)$$

with the constraint $\sum_{C \in L} \delta_{LC} = 1$.

Let $\mathbf{\Phi}$ be the parameter set of Gaussian distributions ($\mu_C, \sigma_C, C \in X$) and the mixture proportions of different components ($\delta_{LC}, L \in \Lambda, C \in L$); $\mathbf{\Pi}$ represents the parameters of prior probabilities of all the classes and pixels ($\pi_{iL}, L \in \Lambda, i = 1, 2, \ldots, N$). With the symbols defined above, the MCGM
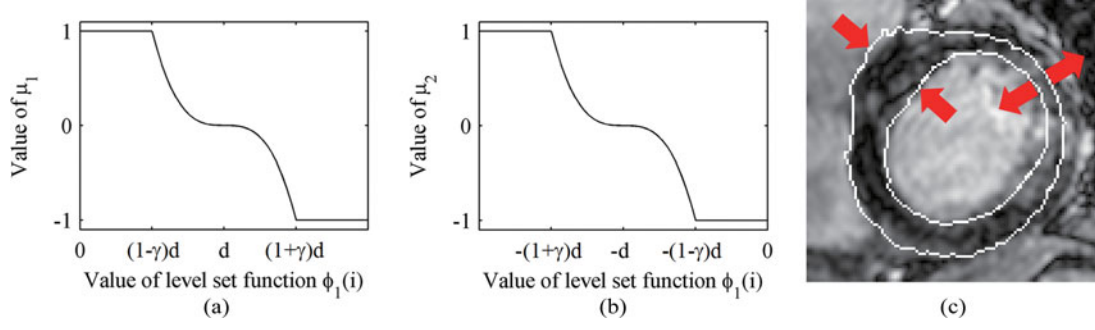
Fig. 4. Explanation of the coupling term in the CLS energy function. (a) the change of $\mu_1$ with respect to the distance to the outer contour represented with $\phi_2(i)$; (b) the change of $\mu_2$ with respect to the distance to the inner contour represented with $\phi_1(i)$; (c) the effect of the coupling term indicated by the red arrows.

model is then given by:

$$f(y_i | \mathbf{\Phi}, \mathbf{\Pi}) = \sum_{L \in \Lambda} \pi_{iL} \sum_{C \in L} \delta_{LC} \phi_{iC}. \tag{3}$$

### B. Expectation Maximization for Model Fitting

**1) Expectation Maximization Algorithm:** To determine the class labels, the parameter sets, $\mathbf{\Phi}$ and $\mathbf{\Pi}$, must be estimated. We adopt the EM algorithm to find the maximum likelihood estimation of the parameters in $\mathbf{\Phi}$. Since there is a one-to-one correspondence between all the components and Gaussian distributions, we take the component labels $z_i \in X$ as the hidden data. The hidden data and the observed image intensity, together form the complete data. An assumption is made that the intensities of all the pixels should be conditionally independent.

We use the EM algorithm to iteratively estimate the *a posteriori* probabilities of each value of the hidden data $z_i$, and model parameters $\mathbf{\Phi}$. Here, the values of the prior probabilities in $\mathbf{\Pi}$ are fixed in the EM steps, and the update of $\mathbf{\Pi}$ is described in Section II-C2). We denote $\mathbf{\Phi}^{(t)}$ as the estimation of $\mathbf{\Phi}$ at the $t$-th iteration. Let $\phi_{iC}^{(t)}$ be the Gaussian value calculated with parameters estimated in the t-th iteration. The E-step provides the conditional expectation of the log likelihood of the complete data $Q(\mathbf{\Phi}|\mathbf{\Phi}^{(t)}) = E[\mathbf{log}p(y, z|\mathbf{\Phi}, \mathbf{\Pi})|y, \mathbf{\Phi}^{(t)}, \mathbf{\Pi}]$ by calculating the posterior probability:

$$p_{iC}^{(t)} = \frac{\pi_{iL} \delta_{LC}^{(t)} \phi_{iC}^{(t)}}{\sum_{L \in \Lambda} \pi_{iL} \sum_{C \in L} \delta_{LC}^{(t)} \phi_{iC}^{(t)}}. \tag{4}$$

The M-step obtains the new estimate of $\mathbf{\Phi}$ that maximizes $Q(\mathbf{\Phi}|\mathbf{\Phi}^{(t)})$, i.e $\mathbf{\Phi}^{(t+1)} = \text{argmax}_{\mathbf{\Phi}} Q(\mathbf{\Phi}|\mathbf{\Phi}^{(t)})$. And the specific updating equation is:

$$\mu_C^{(t+1)} = \frac{\sum_{i=1}^{N} p_{iC}^{(t)} y_i}{\sum_{i=1}^{N} p_{iC}^{(t)}}, \tag{5}$$

$$\left(\sigma_C^{(t+1)}\right)^2 = \frac{\sum_{i=1}^{N} p_{iC}^{(t)} \left(y_i - \mu_C^{(t)}\right)^2}{\sum_{i=1}^{N} p_{iC}^{(t)}}, \tag{6}$$

$$\delta_{LC}^{(t+1)} = \frac{\sum_{i=1}^{N} p_{iC}^{(t)}}{\sum_{C \in L} \sum_{i=1}^{N} p_{iC}^{(t)}}. \tag{7}$$

**2) Initialization of parameters:** A proper initialization is important in the EM algorithm. We register an atlas, containing heart images and corresponding labels of the LV, myocardium and background, to the target DE image. The atlas is pre-constructed using training data of a healthy volunteer and the same atlas is used for the segmentation of different data sets. The labels, $\{L_{\text{atlas}}\}$ determined by the propagated atlas, are used to initialize the parameters [21], [31], as follows:

$$\pi_{iL} = \frac{\exp\left(-\alpha d_{i,L}\right)}{\sum_{L \in \Lambda} \exp\left(-\alpha d_{i,L}\right)}, \tag{8}$$

$$\mu_C^{(0)} = \mu_L - \sigma_L + \frac{2\left(j_C - 1\right)\sigma_L}{|L| - 1}, C \in L, \tag{9}$$

$$\left(\sigma_C^{(0)}\right)^2 = \frac{(\sigma_L)^2}{|L|}, \tag{10}$$

$$\delta_{LC}^{(0)} = \frac{1}{|L|}. \tag{11}$$

Here, $d_{i,L}$ represents the shortest Euclidean distance between pixel $i$ and the pixel sets currently labeled as $L$. The parameter $\alpha$, which controls how blurry the prior probability map is, is determined with our experimental experience. The total number of components in class $L$ is denoted by $|L|$; $j_C$, ranging from 1 to $|L|$, is the index of components in the class $L$; $\mu_L$ and $(\sigma_L)^2$ are the mean and variance for class $L$, which can be estimated as $\mu_L = \sum_{i=1}^{N} \pi_{iL} y_i / \sum_{i=1}^{N} \pi_{iL}$ and $(\sigma_L)^2 = \sum_{i=1}^{N} \pi_{iL} (y_i - \mu_L)^2 / \sum_{i=1}^{N} \pi_{iL}$. The means for components in class $L$ are initialized to be uniformly distributed in the interval $[\mu_L - \sigma_L, \mu_L + \sigma_L]$ as in (9).

### C. Shape Regularization Imposed via Coupled Level Set

**1) Introduction of Coupled Level Set Concept:** As mentioned previously, the intensity range of myocardium overlaps that of the surrounding tissues, which cannot be differentiated from each other based merely on their intensities. The MCGM model presented in Section II-A tackles the problem caused by the intensity heterogeneity. However, the EM framework does not include spatial information. As a result, the healthy myocardium and part of the adjacent tissues, such as liver, may be classified as one component. Similarly,

the MI could be misclassified as blood pool. We therefore introduce the CLS to impose shape regularization on the class prior probability $\pi_{iL}$, based on the donut shape of myocardium in the short-axis slices.

In the literature, Han *et al.* [28] construct the level set energy function based on the posterior probability updated in the EM iteration, and a bending-rate term is also added to maintain the smoothness of the contour. We borrow the posterior probability based term in this work, and build a new CLS energy function.

If the CLS is evolved only based on the posterior probability, the post-regularization process does not include any other form of information extracted from image intensity, and thus may affect the intensity-based classification result after the CLS evolution. In this situation, the CLS step may counteract the classification improvement during the EM steps, when regularizing the posterior probability to maintain the donut shape. As a result, if the prior probability is not accurately initialized, the framework may generate inaccurate segmentation results. To tackle this problem, we propose an extra force to pull the CLS towards the actual myocardium contours, thereby providing a better prior probability for the succeeding EM estimation iteration and accelerate the evolution to the desired results. This is achieved by adding an image intensity-based energy term into the CLS.

*2) Formulation of the Coupled Level Set:* In our work, the CLS contains two contours, with the inner one representing the endocardium and the outer one representing the epicardium. The two contours are evolved simultaneously, and a coupling energy is added to control the relative distance between them, as the thickness of myocardium has a limited variation within a slice. Since the DE images do not contain the entire heart and there are misalignments between the slices, we choose to evolve a 2D CLS on a slice-by-slice basis. The total driving force function of the CLS includes the image intensity term, the posterior probability term, and the coupling term. The driving force of $\phi_k$, $k \in \{1, 2\}$ can be represented as follows:

$$F_k(\phi_1, \phi_2) = \lambda F_{\text{ints},k}(\phi_1, \phi_2) + \upsilon F_{\text{prob},k}(\phi_1, \phi_2)$$
$$+ F_{\text{coup},k}(\phi_1, \phi_2), \qquad (12)$$

where $\lambda$ and $\upsilon$ are weighting parameters, and $\phi_1$ and $\phi_2$ are the level set functions of the two contours respectively. The signed distance function is used as the level set function, with positive inside and negative outside.

In the image intensity term, we adopt the geodesic active contour (GAC) model, which contains both the local edge information in the image and the smoothness constraint of the contours. The energy function is designed as follows, and the corresponding driving forced $F_{\text{ints},k}(\phi_1, \phi_2)$, $k \in \{1, 2\}$ can be obtained by calculating corresponding Euler-Lagrange equations.

$$E_{\text{ints}}(\phi_1, \phi_2) = \int_\Omega g\delta(\phi_1) |\nabla\phi_1| dx + \int_\Omega g\delta(\phi_2) |\nabla\phi_2| dx, \qquad (13)$$

where $g = 1/(1 + |\nabla G_\sigma * Y|^2)$ is the edge stopping function, $G_\sigma$ is the Gaussian kernel with standard deviation $\sigma$, $\Omega$ denotes the 2D image space, and the integral over $\Omega$ denotes that the energy is calculated with all the pixels in the image.

In order to induce the posterior probability term of driving forces, the corresponding energy term is defined as follows,

$$E_{\text{prob}}(\phi_1, \phi_2) = -\int_\Omega p_{\text{LV}} H(\phi_1) H(\phi_2) dx$$
$$- \int_\Omega p_{myo} [1 - H(\phi_1)] H(\phi_2) dx$$
$$- \int_\Omega p_b [1 - H(\phi_1)] [1 - H(\phi_2)] dx, \qquad (14)$$

where $p_L$ $(L \in \{L_{\text{LV}}, L_{myo}, L_b\})$ is the function of position $x$ in 2D image. This term makes use of the posterior probability of the three classes. For pixel $i$, $p_L(i)$ is the currently estimated posterior probability of pixel $i$ belonging to class $L$ from the EM framework. Similarly, the driving force $F_{\text{prob},k}(\phi_1, \phi_2)$, $k \in \{1, 2\}$ can be represented with the corresponding Euler-Lagrange equation.

The coupling term is composed of two terms determining the evolution directions of the two contours respectively:

$$E_{\text{coup}}(\phi_1, \phi_2) = \int_\Omega \mu_1 H(\phi_1) dx + \int_\Omega \mu_2 H(\phi_2) dx, \qquad (15)$$

where $H(\cdot)$ is the Heaviside function $H(n) = \left\{ \begin{smallmatrix} 0, & n<0 \\ 1, & n\geq0 \end{smallmatrix} \right.$. The inner contour shrinks when the parameter $\mu_1$ is positive, and expands when $\mu_1$ is negative. Similarly, the outer contour is controlled by parameter $\mu_2$.

Synthesizing the three terms of the energy function, the two contours are evolved under the driving force:

$$\frac{\partial\phi_1}{\partial t} = \lambda\delta(\phi_1) div\left(g\frac{\nabla\phi_1}{|\nabla\phi_1|}\right)$$
$$+ \upsilon\delta(\phi_1) \{(p_{\text{LV}} - p_{myo}) H(\phi_2) - p_{ib} [1 - H(\phi_2)]\}$$
$$- \mu_1\delta(\phi_1), \qquad (16)$$

$$\frac{\partial\phi_2}{\partial t} = \lambda\delta(\phi_2) div\left(g\frac{\nabla\phi_2}{|\nabla\phi_2|}\right)$$
$$+ \upsilon\delta(\phi_2) \{p_{i\text{LV}} H(\phi_1) - (p_{myo} - p_b) [1 - H(\phi_1)]\}$$
$$- \mu_2\delta(\phi_2). \qquad (17)$$

In order to get a relatively uniform myocardium thickness, instead of fixed numbers, $\mu_1$ and $\mu_2$ are designed to be spatially varying to impose the thickness constraint. The values of $\mu_1$ and $\mu_2$ are calculated as functions of the distance between pixel $i$ and the two contours, which can be represented as values of the
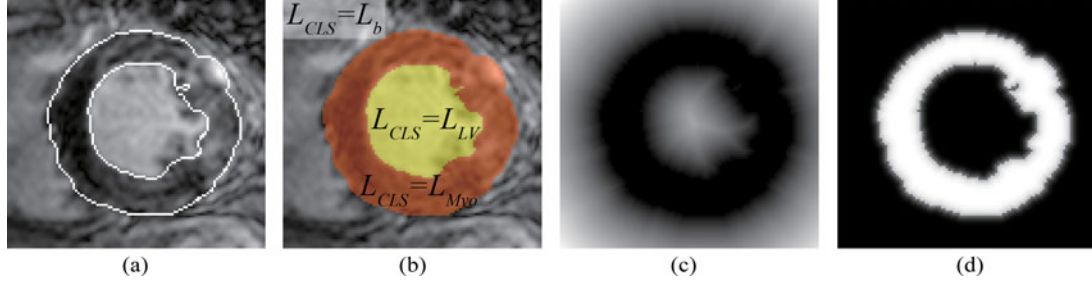
Fig. 5.   Computation of the prior probability with the coupled level set (CLS) scheme. (a) the two contour lines; (b) the three labelled pixel sets according to the contour lines, i.e., the left ventricular cavity ($L_{LV}$), myocardium ($L_{myo}$) and background ($L_{bg}$); (c) the Euclidean distance map of the myocardium pixel set; (d) the prior probability map of the myocardium.

level set functions $\phi_1$, $\phi_2$ [27]:

$$\mu_1\left(\phi_2\left(i\right)\right)$$

$$= \begin{cases} 1 & \phi_2\left(i\right) < \left(1-\gamma\right)d \\ -\left(\frac{\phi_2\left(i\right)-d}{\gamma d}\right)^3 & \left(1-\gamma\right)d \leq \phi_2\left(i\right) \leq \left(1+\gamma\right)d \\ -1 & \phi_2\left(i\right) > \left(1+\gamma\right)d \end{cases} \quad (18)$$

$$\mu_2\left(\phi_1\left(i\right)\right)$$

$$= \begin{cases} 1 & \phi_1\left(i\right) < -\left(1+\gamma\right)d \\ \left(\frac{-\phi_1\left(i\right)-d}{\gamma d}\right)^3 & -\left(1+\gamma\right)d \leq \phi_1\left(i\right) \leq -\left(1-\gamma\right)d \\ -1 & \phi_1\left(i\right) > -\left(1-\gamma\right)d \end{cases}$$

$$(19)$$

where $d$ represents the mean thickness of the myocardium. The parameter $\gamma$, subjects to $0 \leq \gamma < 1$, is the ratio of the myocardium thickness change over the mean thickness $d$. For a pixel $i$ in the inner contour, when the shortest distance from $i$ to the outer contour $\phi_2(i)$ is less than $d$, $\mu_1$ is positive and thus the inner contour tends to shrink in pixel $i$. When $\phi_2(i) > d$, the contour tends to expand in pixel $i$. A similar force is imposed on the outer contour simultaneously.

Thus, the CLS takes evolution under the force generated from both the image intensity gradient and the posterior probability calculated in the current iteration, as shown in (16) and (17). The evolved result is then used to update the prior probability $\pi_{iL}$ for the next iteration of the EM algorithm. The prior probability is estimated with an exponential function according to the pixel's relative position to the contours of CLS:

$$\pi_{iL} = \frac{\exp\left(-\alpha d_{i,L}\right)}{\sum_{L\in\Lambda}\exp\left(-\alpha d_{i,L}\right)}, \quad (20)$$

where $\alpha$ and $d_{i,L}$ are the same as the notations in (8). The labels $\{L_{CLS}\}$ are determined according to the resulting endocardial and epicardial contour lines of the CLS, as Fig. 5(a) and (b) illustrate. Fig. 5(c) and (d) show the distance and prior probability map of the myocardium.

In practice, the method converges well. Upon convergence, the label after shape regularization $\{L_{CLS}\}$ is taken as the final results.

The myocardium segmentation results from the MCGM-CLS framework usually contain part of the papillary muscles, which are located close to myocardium and have similar intensity.

TABLE I
THE DETAILS OF THE DATA SETS

| Number of subjects | Slice resolution | Pixel spacing | Number of slice | Slice thickness |
|---|---|---|---|---|
| 33 | $490 \times 490$ | 0.7292 mm | 10–18 | 5 mm |

However, for medical diagnostic purposes, the papillary muscles are generally excluded from the myocardium. Therefore we compute the convex hull of the inner contour, and use interpolation to include the papillary muscles into the LV class in each slice.

## III. RESULTS AND DISCUSSION

### A. Data

Thirty-three DE MRI data sets from patients with MI were acquired in our institution for this study, which had the approval from the institutional review board. Each data set comprises 10-18 short axis slices, as shown in Table I. All the slices, including the apical and basal ones, were used to test the proposed method.

We randomly split the data sets into 3 subsets, each subset containing 11 data. One subset was used to tune the parameters of the proposed method and the compare methods, and the rest two were used to evaluate the final results. All the three subsets were used to show the sensitivity of the parameters to different datasets.

The manual segmentation of myocardium was provided by an expert for all the 33 data sets, and was considered as the ground truth. In order to evaluate the inter-observer variability, we randomly selected 11 subjects for another manual segmentation, which was performed by a well-trained biomedical engineering student who was unaware of the methodology of this work.

### B. Evaluation Metrics

To quantitatively measure the accuracy of the proposed segmentation method, we adopted the Dice similarity coefficient (DSC) and average surface distance (ASD). DSC measures the overlap between the segmentation results of the tested method and the ground truth, defined as $\text{DSC}(S_a, S_m) = [2|S_a \cap S_m|/(|S_a| + |S_m|)] \cdot 100\%$, where $S_a$ and $S_m$ are the
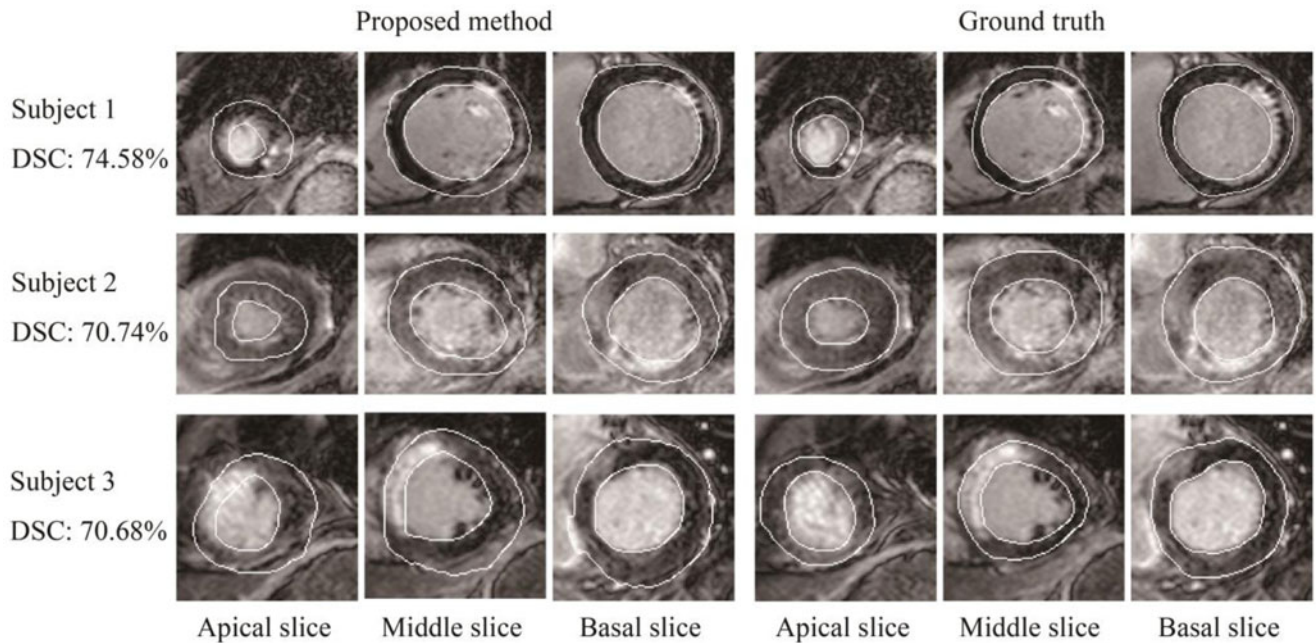
Fig. 6. Demonstration of typical examples: three cases using the proposed segmentation method and the corresponding ground truth on the apical, middle and basal slices.

automatic segmentation and the ground truth of the target region respectively.

ASD measures the average Euclidean distance between the segmented contours and the ground truth. For every point in a segmented contour, the Euclidean distance to the nearest point in corresponding ground truth contour was calculated in a slice by slice manner, and then the distance was averaged within each data set.

To examine the correlation and agreement between the proposed method and the manually delineated ground truth, we also provided the regression line and the Bland-Altman plot. The volume encountered by the endocardium and epicardium were calculated in each data set according to the segmentation results and ground truth respectively. The Pearson correlation coefficient (PCC) was also calculated: $\text{PCC} = (\text{Cov}(V_a, V_b))/\sqrt{(\text{Var}(V_a)\text{Var}(V_b))}$, where $V_a$ and $V_b$ are the calculated volumes of automatic segmentation and ground truth. The notation $\text{Cov}(V_a, V_b)$ represents the covariance of $V_a$ and $V_b$; $\text{Var}(V_a)$ and $\text{Var}(V_b)$ represent the variance of $V_a$ and $V_b$ respectively. The value of PCC is between $-1$ and $+1$, where 1 indicates total positive correlation and 0 implies no correlation.

### C. Studies

**1) Effectiveness of Proposed Techniques and Inter-Observer Study:** Fig. 6 displays the typical results of apical, middle and basal slices from 3 data sets, where the white curves represent the endocardium and epicardium. The segmentation of apical slices is worse than that of the middle and basal slices, because of their relative low contrast and variable positions.

Three new ideas, i.e. the multi-component Gaussian mixture (MCGM) for tackling intensity heterogeneity, the coupled level set (CLS) for imposing shape priors, and the image intensity based force (IBF) for improving CLS, are introduced into the EM-based framework to achieve the fully automatic segmentation of myocardium from the DE MRI. To study the strength of the overall method and the effect of each technique, we compare six segmentation schemes, as follows:

1) *MCGM+CLSIBF:* This is **the proposed method** in which the parameters of the MCGM-based EM framework are initialized from the propagated atlas and the IBF is introduced into the CLS.

2) *MCGM+CLS:* This method adopts the atlas propagation and the CLS constrained EM framework, similar to the proposed method, but the implementation of the CLS does not include the image intensity term proposed in (13). This method is used to evaluate the efficacy of the image information in the adopted GAC model.

3) *MCGM+Atlas:* This method employed the MCGM-based EM estimation framework [21]. Compared to *MCGM+CLS*, the CLS is substituted by the propagated atlas used in the initialization step. Also, to reduce the influence of noise and impose continuity to the final segmentation, this method adopts the Markov Random Field (MRF) [31], [32], and the prior probability $\pi_{iL}$ is the product of estimated probability form the MRF and that from atlas propagation. The final labels are determined as those providing the maximum posterior probability. We employ this method for evaluating the effect of the introduced CLS, compared with the conventional method, in imposing spatial information and fitting to the images.

4) *CV+CLSIBF:* This method is the standard region based level set method, incorporated with the same coupling term and intensity term as the proposed method. In the region based level set, the intensity distribution in each

TABLE II
THE ACCURACY OF SEGMENTATION RESULTS COMPARED TO MANUAL
SEGMENTATION EVALUATED WITH DSC (%)

| Methods | Endocardium | Epicardium | Myocardium |
|---|---|---|---|
| Atlas Seg | $85.61 \pm 6.24$ | $89.35 \pm 3.41$ | $66.11 \pm 5.75$ |
| MCGM+Atlas | $87.17 \pm 6.06$ | $89.82 \pm 2.97$ | $71.50 \pm 5.26$ |
| MCGM+CLS | $87.32 \pm 5.50$ | $90.43 \pm 3.48$ | $73.50 \pm 5.99$ |
| CV+CLSIBF | $86.81 \pm 5.33$ | $90.02 \pm 3.56$ | $72.19 \pm 6.56$ |
| GrabCut+Atlas | $83.43 \pm 7.81$ | $88.20 \pm 4.31$ | $73.46 \pm 5.07$ |
| MCGM+CLSIBF | $87.43 \pm 5.62$ | $90.53 \pm 3.20$ | $73.58 \pm 5.58$ |
| Inter-observer | $88.56 \pm 5.14$ | $91.57 \pm 3.77$ | $73.10 \pm 8.10$ |

Note that the inter-observer difference is evaluated on 11 data sets.

TABLE III
THE ACCURACY OF SEGMENTATION RESULTS COMPARED TO MANUAL
SEGMENTATION EVALUATED WITH ASD (MM)

| Methods | Endocardium | Epicardium |
|---|---|---|
| Atlas Seg | $3.19 \pm 1.35$ | $3.21 \pm 0.96$ |
| MCGM+Atlas | $2.80 \pm 1.28$ | $3.20 \pm 0.91$ |
| MCGM+CLS | $2.65 \pm 1.05$ | $2.89 \pm 0.92$ |
| CV+CLSIBF | $2.73 \pm 0.96$ | $3.01 \pm 0.95$ |
| GrabCut+Atlas | $2.70 \pm 0.99$ | $3.38 \pm 0.96$ |
| MCGM+CLSIBF | $2.65 \pm 1.10$ | $2.88 \pm 0.87$ |
| Inter-observer | $2.64 \pm 1.13$ | $2.72 \pm 1.36$ |

Note that the inter-observer difference is evaluated on
11 data sets.

class can be taken as being modeled with single Gaussian
function and without prior probability. We added this
method to evaluate the effect of the MCGM.

5) *GrabCut+Atlas:* We choose the GrabCut as a compared
method to examine the results of the proposed method.
However, as the standard GrabCut method does not con-
tain any spatial constraint, reasonable results cannot be
achieved in many cases. So a GrabCut method using
probabilistic atlas is adopted [33], and in this paper, the
propagated atlases are used to build the probabilistic map
in the same way as initializing class prior probability.
The edges in the GrabCut segmentation are smoothed
and considered as the final results.

6) *Atlas Seg:* The conventional atlas-based segmentation us-
ing image registration and atlas propagation.

The final endocardial contours in the above mentioned meth-
ods are achieved via convex hull computation and interpolation
except **Atlas Seg** and **GrabCut+Atlas.** The registration in all
the six methods consists of three steps, i.e. global affine registra-
tion for localization of the whole heart, locally affine registration
method for initialization of substructures such as the four cham-
bers and great vessels, and free-form deformation registration
for refinement of local details [30]. The resultant transformation
is then used to transform the atlas into the image space of the
target DE MR image.

For each method, the parameters which give the best per-
formance on subset 1 are chosen. The DSC and ASD for the
six methods are calculated over the 22 subjects in the rest two
subsets, which are shown in Tables II and III respectively. The
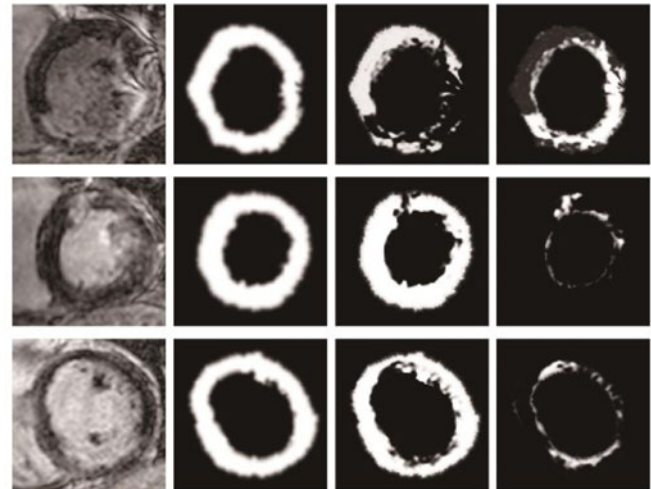results of inter-observer variability are also provided.



Fig. 7. The posterior probability map of myocardium and its two
components.

The methods of **Atlas Seg**, **GrabCut+Atlas,** and
**CV+CLSIBF** are the variants of the conventional segmentation
methods. The proposed method outperformed these three meth-
ods in both the DSC and ASD metric. The difference between the
results by the proposed method and ground truth segmentation
is close to the inter-observer variability, which demonstrates
the strength of the proposed method. It is worth mentioning
that even though the myocardial DSC of GrabCut+Atlas is
comparable to that of the proposed method, the epi- and endo-
cardial DSCs of GrbCut+Atlas are evidently lower than the pro-
posed method with statistical significance (DSC of epicardium:
$88.20 \pm 4.31\%$ for GrabCut+Atlas and $90.53 \pm 3.20\%$ for
the proposed method, p $= 0.00027$; DSC of epicardium:
$83.43 \pm 7.81\%$ for GrbCut+Atlas and $87.43 \pm 5.62\%$ for the
proposed method, p $= 0.00129$). The relatively good myocar-
dial DSC of GrabCut+Atlas is probably due to the fact that
we used the myocardial DSC as the metric to tune the param-
eters. Furthermore, the elongated shape of myocardium leads
to the relative small area and long contours, which results in a
situation where the GrabCut+Atlas method trends to classify
a larger myocardium area than the ground truth. This leads to
a relatively better myocardial DSC of GrabCut+Atlas, but the
results can be problematic in practice. By contrast, the proposed
method, making use of the mean myocardium thickness and
relative thickness change estimated with the statistical anatomy
data, can mitigate this problem.

From the DSC of myocardium, one can observe that
the propagated atlas provides a relatively poor segmentation
(DSC: $66.11 \pm 5.75\%$). This is because that the registration
between the atlas and the target DE image is challenged by the
existence of MI. Similar problems are seen in related work, for
example in [20], though the strong prior information of the cine
MRI of the same patient is used, manual intervention is required
to guarantee a robust registration between the cine and the DE
MRI.

The effectiveness of MCGM is first examined. Com-
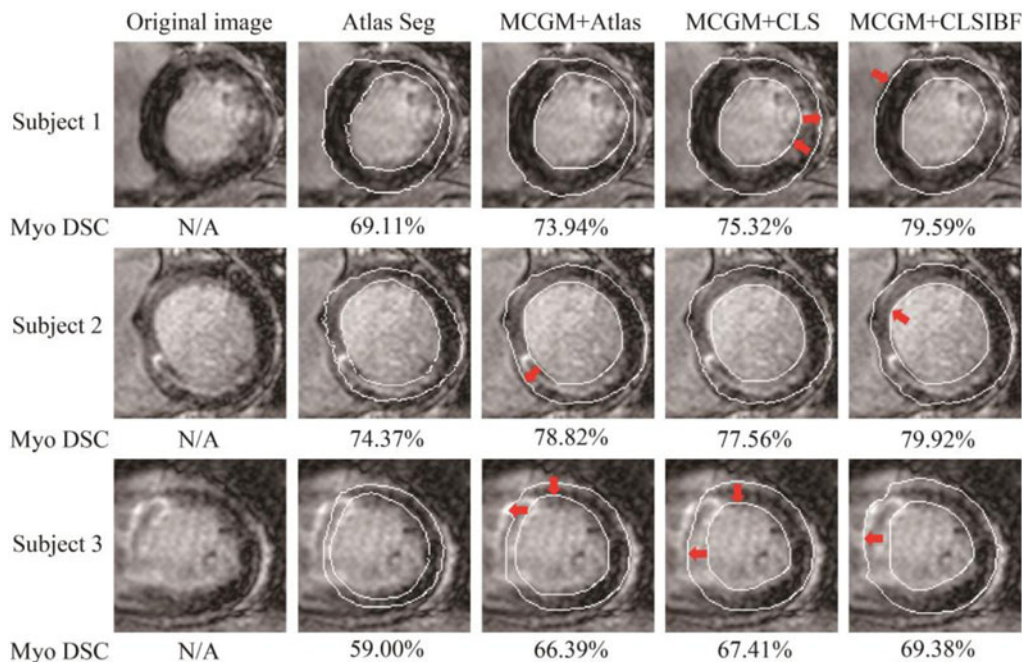pared to the **Atlas Seg**, the **MCGM+Atlas** method achieves

Fig. 8.    Three typical results of the proposed method and three compared methods. The red arrows indicates the improvements compared to the results demonstrated in its left. The DSC of myocardium is shown below each image.

significant improvements ($p < 0.01$). This shows that, with the propagated atlas as a spatial regulation, the MCGM can give a good description of the intensity distribution of the DE images and thus improve the segmentation performance. Also, the proposed method gives better results than **CV+CLSIBF** method ($p < 0.05$). This is owing to the ability of **MCGM** to model the heterogeneous intensity distribution in myocardium, which cannot be done with a simple Gaussian function in **CV+CLSIBF**. To further visualize the effect of MCGM, we provide the posterior probability maps of myocardium components in Fig. 7.

Then, the effectiveness of MCGM is examined. The **MCGM+CLS** method further significantly improves the segmentation to $73.50 \pm 5.99\%$ ($p < 0.01$) compared to **MCGM+Atlas**. For visual illustration of the effect of the CLS, some typical results of three compared methods and the proposed methods are showed in Fig. 8. Conventionally, the propagated atlas is used as a fixed regularization, which limits the flexibility of the segmentation algorithm, since the propagated atlas may provide inaccurate myocardium spatial information. For example, the **MCGM+CLS** result of subject 3 in Fig. 8, as indicated by the arrows, the CLS corrects the inaccurate delineation of myocardium from the atlas propagation, while the **MCGM+Atlas** method fails. Apart from its adaptability, the CLS also introduces extra information, i.e. the myocardium thickness constraint, to regularize the shape in the segmentation results. Such as in subject 1 in Fig. 8, part of the myocardium in the **MCGM+Atlas** result is too thin to be realistic.

Finally, the proposed method achieves a DSC of $73.58 \pm 5.58\%$. Although compared to **MCGM+CLS** the increase in the DSC is minor over all the 22 data, however, better delineation of the myocardial boundaries can be observed when the clear edges can be detected, as shown in Fig. 8. The case of subject 3
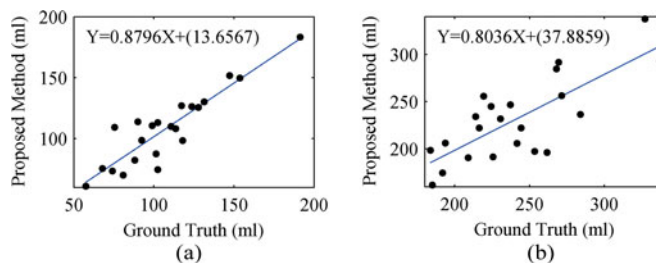


Fig. 9.    The regression line of the proposed method and ground truth. (a) volume encountered by endocardium; (b) volume encountered by epicardium.

illustrates that when the probability-based MCGM-CLS system becomes trapped in an undesired local optimum, the introduced image intensity-based force becomes crucial in correcting the segmentation.

The ASD of endocardium is smaller than that of epicardium in all the method, probably because the tissue around the endocardium is simpler (only blood and myocardium), thus the boundary is easier to be delineated. However, the DSC of endocardium is smaller than epicardium, probably because the value of DSC tends to be greater when the evaluated area is larger.

*2) Agreement of the Proposed Method With the Ground Truth:* The regression line and Bland-Altman plot are shown in Figs. 9 and 10. The regression line shows that the segmentation of endocardium (PCC: 0.90) is better correlated with the ground truth than the epicardium (PCC: 0.77), which is in accordance with the low endocardial ASD.

In the Bland-Altman plot, we examine the subject corresponding to the point outside the 2SD lines (red lines in Fig. 10). In this case, part of the infarcted myocardium is misclassified as
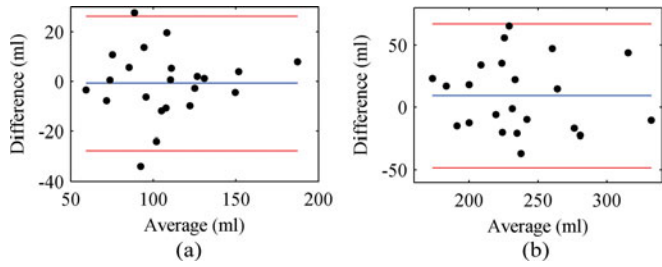
Fig. 10. The Bland-Altman plot of the proposed method and ground truth. (a) volume encountered by endocardium; (b) volume encountered by epicardium.
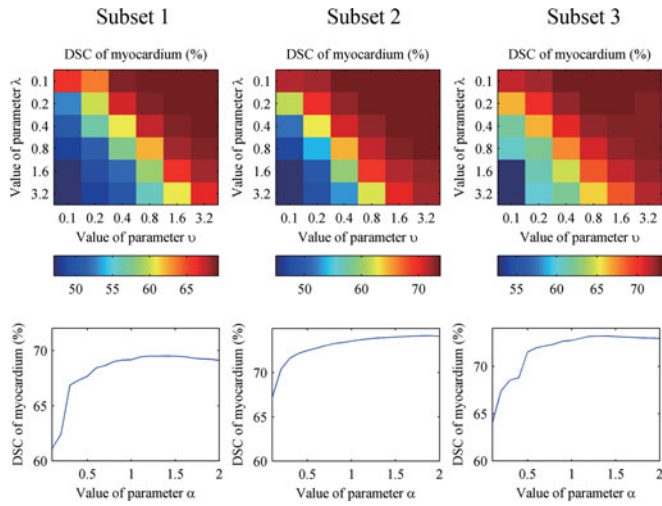


Fig. 11. The effect of the parameters on average DSC on three subsets.

blood pool in middle slice. At the same time, the apical slices also suffer from an incorrect detection of the myocardium.

*3) Determination of Parameters:* In the proposed method, the parameters $d$ and $\gamma$ have physical meanings, i.e. the mean thickness and relative thickness change of myocardium, and can be estimated using the statistical anatomy data. The appropriate values of the energy function weighting parameters $\lambda$ and $\upsilon$, and the prior probability parameter $\alpha$ are tuned on the subset 1. Particularly, Parameters $\lambda$ and $\upsilon$ are jointly tuned.

To demonstrate the sensitivity of the parameters to different datasets, the way DSC varies with parameters is showed on not only the subset 1, but all the three subsets. As shown in Fig. 11, the best values for the parameters are accordant in the three subsets.

The first row in Fig. 11 shows how the average DSC of myocardium varies with respect to the different values of parameter $\lambda$ and $\upsilon$ on the three subsets. The best myocardium DSC is achieved when $\lambda$ is around 0.1–0.2 and $\upsilon$ between 0.8 and 1.6. The relative small value of $\lambda$ indicates that the boundaries of myocardium is indistinct in DE MRI. The DSC drops dramatically when $\lambda$ increases and $\upsilon$ decreases, while it remains stable with a slow decrease in the opposite case. This indicates that a relative large intensity gradient based force may leading the contour to disturbing edges, while a relative small force can help refine the results.

## TABLE IV
### THE RESULTS REPORTED IN THE LITERATURE

| Reference | Data | ASD | DSC (%) |
|---|---|---|---|
| **Dikici *et al.* 2004** | 42 slices | Endo and Epi: 1.54 ± 0.39 pixels (pixel size of 1.5 mm) | N/A |
| **Ciofolo *et al.* 2008** | 27 subjects | Endo: 2.2 ± 0.6 mm Epi: 2.0 ± 0.8 mm | N/A |
| **Wei *et al.* 2013** | 21 subjects | Endo: 0.94 ± 0.44 mm, 1.51 ± 0.74 mm Epi: 0.90 ± 0.41 mm, 1.68 ± 0.70 mm | Endo: 95.33 ± 3.63, 92.64 ± 4.36 Epi: 96.88 ± 1.84, 94.35 ± 2.70 Myo: 88.57 ± 4.75, 82.32 ± 5.59 |
| **Ours** | 33 subjects | Endo: 2.70 ± 0.94 mm Epi: 2.98 ± 0.89 mm | Endo: 86.74 ± 5.82 Epi: 90.40 ± 3.17 Myo: 73.77 ± 5.56 |

Note that Wei *et al.* (2013) evaluated the results with two sets of manual segmentations. Endo, Epi and Myo represent endocardium, epicardium and myocardium respectively.

The variation of average DSC of myocardium as a function of the parameter $\alpha$ is plotted in second row in Fig. 11. The proposed method achieves the best segmentation results when $\alpha$ is 1.4. And the average DSC drops dramatically when the value of $\alpha$ become smaller, since the shape regularization is not efficiently imposed. While the decrease of average DSC is relatively slow when the value of $\alpha$ become larger, in which situation the imposed shape regularization is too strong to achieve further improvement.

Finally, our segmentation program is built on Matlab with non-optimized code and performed on a personal computer equipped with Intel E5200 2.50 GHz processor and 2GB RAM. The runtime from the initialization of parameters (after registration was performed) to the accomplishment of convex hull computation is recorded. The average runtime for one subject is $1.26 \pm 0.43$ minutes. The registration tools are implemented in C++ and downloaded from the ZXHPROJ webpage [34]. The computation time of the registration is $6.03 \pm 1.60$ minutes.

*4) Results in the Literature:* We list the segmentation results of DE MRI reported in the literature for reference (Table IV). As we mainly focus on myocardial segmentation, only those studies with quantitative evaluation of myocardium segmentation are shown. It should be noted that an objective inter-study comparison is difficult, since the data sets and implementation can be different.

All the three studies reported in the literature make use of the segmentation of cine MRI, which provides strong prior information for the segmentation of DE MRI. In the work of Wei *et al.* [20], manual registration was introduced when the automatic translational registration failed on certain slices. By contrast, our approach takes single predefined atlas and is fully automatic. The results of [20] were evaluated with two sets of manual segmentation, and the reported inter-observer agreement was much higher: the DSC for myocardium of the two manual segmentation sets is $82.93 \pm 5.28\%$, and ASD for endocardium and epicardium are respectively $1.46 \pm 0.66$ mm, $1.56 \pm 0.58$ mm. This indicates the difference, in terms of difficulty of performing myocardium segmentation, between their datasets and ours.

## IV. CONCLUSION AND FUTURE WORK

In this work, we have explored the possibility of delineating the myocardium from DE MRI, employing a fully automatic framework. The image intensity is modeled with a MCGM model, and the parameters are estimated using the EM algorithm. A CLS, with probability, intensity and coupling terms, is introduced into the iteration to impose a spatial regularization to the prior probabilities.

As the results demonstrate, the propagated atlases provide a relative poor initial estimation of the myocardium. The shape of the heart can be very different between the atlas and the target DE MRI, making it difficult to achieve an accurate registration between them. Furthermore, with the irregular infarct patterns and relative low contrast of DE images, the recovering of accurate myocardium contours becomes particularly challenging. In the context of clinical practice, the DE and T2 MRI of the MI patients are usually analyzed simultaneously to evaluate both the MI and edematous regions. Therefore, in future work we will combine the complementary information from the T2 and DE cardiac MRI within a unified framework, and perform the segmentation on the two sequences simultaneously. Also, in this paper, we mainly focus on the segmentation of myocardial infarction cases. In the future work, we plan to collect more data and evaluate the proposed method in different datasets with various pathologies and cardiac conditions.

## REFERENCES

[1] A. S. Flett *et al.*, "Evaluation of techniques for the quantification of myocardial scar of differing etiology using cardiac magnetic resonance," *J. Amer. Coll. Cardiology Imag.*, vol. 4, no. 2, pp. 150–156, Feb. 2011.

[2] A. Kolipaka *et al.*, "Segmentation of non-viable myocardium in delayed enhancement magnetic resonance images," *Int. J. Cardiology Imag.*, vol. 21, no. 2–3, pp. 303–311, Apr. 2005.

[3] L. C. Amado *et al.*, "Accurate and objective infarct sizing by contrast-enhanced magnetic resonance imaging in a canine myocardial infarction model," *J. Am. Coll. Cardiology*, vol. 44, no. 12, pp. 2383–2389, Dec. 21, 2004.

[4] M. K. Metwally *et al.*, "Improved technique to detect the infarction in delayed enhancement image using k-mean method," in *Image Analysis and Recognition*: Berlin, Germany: Springer-Verlag, 2010, pp. 108–119.

[5] V. V. Vanya, "Automatic quantification of myocardial infarction from delayed enhancement MRI," in *Proc. Int. Conf. Signal-Image Technol. Internet-Based Syst.*, 2011, pp. 277–283.

[6] N. Kachenoura *et al.*, "Robust assessment of the transmural extent of myocardial infarction in late gadolinium-enhanced MRI studies using appropriate angular and circumferential subdivision of the myocardium," *Eur. Radiol.*, vol. 18, no. 10, pp. 2140–2147, Oct. 2008.

[7] K. Elagouni *et al.*, "Automatic segmentation of pathological tissues in cardiac MRI," in *Proc. IEEE Int. Symp. Biomed. Imag.*, 2010, pp. 472–475.

[8] A. Hennemuth *et al.*, "A comprehensive approach to the analysis of contrast enhanced cardiac MR images," *IEEE Trans. Med. Imag.*, vol. 27, no. 11, pp. 1592–1610, Nov. 2008.

[9] A. Hennemuth *et al.*, "Mixture-model-based segmentation of myocardial delayed enhancement MRI," in *Statistical Atlases and Computational Models of the Heart. Imaging and Modelling Challenges*, Berlin, Germany: Springer-Velag, 2013, pp. 87–96.

[10] E. Heiberg *et al.*, "Automated quantification of myocardial infarction from MR images by accounting for partial volume effects: animal, phantom, and human study," *Radiol.*, vol. 246, no. 2, pp. 581–588, Feb. 2008.

[11] Q. A. Tao *et al.*, "Automated segmentation of myocardial scar in late enhancement MRI using combined intensity and spatial information," *Magn. Reson. Med.*, vol. 64, no. 2, pp. 586–594, Aug. 2010.

[12] X. Zhuang, "Challenges and methodologies of fully automatic whole heart segmentation: A review," *J. Healthcare Eng.*, vol. 4, no. 3, pp. 371–408, 2013.

[13] C. Petitjean and J.-N. Dacher, "A review of segmentation methods in short axis cardiac MR images," *Med. Image Anal.*, vol. 15, no. 2, pp. 169–184, 2011.

[14] A. Pednekar *et al.*, "Automated left ventricular segmentation in cardiac MRI," *IEEE Trans. Biomed. Eng.*, vol. 53, no. 7, pp. 1425–1428, Jul. 2006.

[15] H. F. Hu *et al.*, "Hybrid segmentation of left ventricle in cardiac MRI using gaussian-mixture model and region restricted dynamic programming," *Magn. Reson. Imag.*, vol. 31, no. 4, pp. 575–584, May 2013.

[16] M. Rajchl *et al.*, "Interactive hierarchical-flow segmentation of scar tissue from late-enhancement cardiac MR images," *IEEE Trans. Med. Imag.*, vol. 33, no. 1, pp. 159–172, Jan. 2014.

[17] E. Dikici *et al.*, "Quantification of delayed enhancement MR images," in *Proc. Med. Image Comput. Comput.-Assisted Intervention*, 2004, pp. 250–257.

[18] R. El Berbari *et al.*, "An automated quantification of the transmural myocardial infarct extent using cardiac DE-MR images," in *Proc. Annu. Int. Conf. IEEE Eng. Med. Biol. Soc.*, 2009, pp. 4403–4406.

[19] C. Ciofolo *et al.*, "Automatic myocardium segmentation in late-enhancement MRI," in *Proc. IEEE Int. Symp. Biomed. Imag.*, 2008, pp. 225–228.

[20] D. Wei *et al.*, "Three-dimensional segmentation of the left ventricle in late gadolinium enhanced MR images of chronic infarction combining long-and short-axis information," *Med. Image Anal.*, vol. 17, no. 6, pp. 685–697, Aug. 2013.

[21] W. Z. Shi *et al.*, "Automatic segmentation of different pathologies from cardiac cine MRI using registration and multiple component EM estimation," in *Functional Imaging and Modeling of the Heart*, Berlin, Germany: Springer-Veralg, 2011, pp. 163–170.

[22] J. Liu *et al.*, "Myocardium segmentation combining T2 and DE MRI using Multi-Component Bivariate Gaussian mixture model," in *Proc. IEEE Int. Symp. Biomed. Imag.*, 2014, pp. 886–889.

[23] L. A. Vese and T. F. Chan, "A multiphase level set framework for image segmentation using the Mumford and Shah model," *Int. J. Comput. Vis.*, vol. 50, no. 3, pp. 271–293, 2002.

[24] A. Yezzi *et al.*, "A fully global approach to image segmentation via coupled curve evolution equations," *J. Visual Commun. Image Representation*, vol. 13, no. 1, pp. 195–216, Mar. 01, 2002.

[25] X. L. Zeng *et al.*, "Segmentation and measurement of the cortex from 3-D MR images using coupled-surfaces propagation," *IEEE Trans. Med. Imag.*, vol. 18, no. 10, pp. 927–937, Oct. 1999.

[26] N. Paragios, "A variational approach for the segmentation of the left ventricle in cardiac image analysis," *Int. J. Comput. Vis.*, vol. 50, no. 3, pp. 345–362, Dec. 2002.

[27] M. Lynch *et al.*, "Left-ventricle myocardium segmentation using a coupled level-set with a priori knowledge," *Comput. Med. Imag. Graph.*, vol. 30, no. 4, pp. 255–262, Jun. 2006.

[28] H. Han *et al.*, "A unified EM approach to bladder wall segmentation with coupled level-set constraints," *Med. Image Anal.*, vol. 17, no. 8, pp. 1192–1205, Dec. 2013.

[29] X Zhuang and J Shen, "Multi-scale patch and multi-modality atlases for whole heart segmentation of MRI," *Med. Image Anal.*, vol. 31, pp. 77–87, 2016 .

[30] X. Zhuang *et al.*, "A registration-based propagation framework for automatic whole heart segmentation of cardiac MRI," *IEEE Trans. Med. Imag.*, vol. 29, no. 9, pp. 1612–1625, Sep. 2010.

[31] M. Lorenzo-Valdes *et al.*, "Segmentation of 4D cardiac MR images using a probabilistic atlas and the EM algorithm," *Med. Image Anal.*, vol. 8, no. 3, pp. 255–265, Sep. 2004.

[32] K. Van Leemput *et al.*, "Automated model-based tissue classification of MR images of the brain," *IEEE Trans. Med. Imag.*, vol. 18, no. 10, pp. 897–908, Oct. 1999.

[33] X. Zhou *et al.*, "A universal approach for automatic organ segmentations on 3D CT images based on organ localization and 3D GrabCut," in *Proc. SPIE*, vol. 9035, 2014.

[34] X. Zhuang. ZXHPROJ, 2016. [Online]. Available: www.sdspeople. fudan.edu.cn/zhuangxiahai/0/zxhproj/
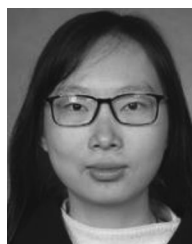
**Jie Liu** is currently working toward the Ph.D. degree in biomedical engineering at Shanghai Jiao Tong University, Shanghai, China. Her research interest is medical image analysis, especially the segmentation of cardiac MRI.
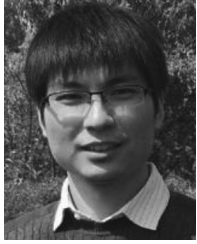
**Xiahai Zhuang** received the Graduate degree from the Department of Computer Science, Tianjin University, Nankai Qu, China, the M.S. degree in computer science from Shanghai Jiao Tong University, Shanghai, China, and the Doctorate degree from University College London, London, U.K. He is an Associate Professor in the School of Data Science, Fudan University, Yangpu Qu, China. His research interests include medical image analysis, image processing, data science, and computer vision.

His works have been nominated twice for the MICCAI Young Scientist Awards (2008, 2012).

**Lian-Ming Wu** received the Med. Master and PhD's degree from the School of medicine, Shanghai Jiaotong University, Shanghai, China, in 2014. He is currently with the Department of Radiology, Renji Hospital.CShanghai Jiao Tong University, Shanghai, China. His research interest focuses on cardiac MRI. He has authored more than 40 peer-reviewed papers.

**Dongaolei An** received the Doctor of Medicine degree from the School of Medicine, Shanghai Jiaotong University, Shanghai, China, in 2016. She mainly studied cardiovascular magnetic resonance for 3 years, and specializes in T1, T2 mapping, and myocardial enhancement.

**Jianrong Xu** received the Med. Master and PhD's degree from School of medicine, Shanghai Jiaotong University, Shanghai, China, in 1990. He is the Director of the Department of Radiology, Renji Hospital.CShanghai Jiao Tong University; Shanghai, China. He is serving as 11 Associate Editors or Chairman of local academic journals or associations and has authored more than 160 peer-reviewed papers. He is holding eight Chinese patents. He has been honored with several national and municipal academic awards.

**Terry Peters** (S'72–M'73–SM'97–F'09–LF'14) is a Scientist in the Imaging Research Laboratories, Robarts Research Institute, London, ON, Canada, and a Professor in the Departments of Medical Imaging and Medical Biophysics at the University of Western Ontario, London, ON, Canada, as well as a member of the Graduate Programs in neurosciences and biomedical engineering. He is also an adjunct Professor at McGill University, Montreal, QC, Canada. He received his graduate training at the University of Canterbury in New Zealand in Electrical Engineering. For the past 30 years, his research has built on this foundation, focusing on the application of computational hardware and software advances to medical imaging modalities in surgery and therapy. Starting in 1978 at the Montreal Neurological Institute, his laboratory pioneered many of the image-guidance techniques and applications for image-guided neurosurgery. In 1997, he was recruited by the Robarts Research Institute, University of Western Ontario to establish a focus of image-guided surgery and therapy within the Robarts Imaging Research Laboratories.

He has authored more than 200 peer-reviewed papers and book chapters, a similar number of abstracts, and has delivered more than 180 invited presentations. He is a Fellow of the Canadian College of Physicists in Medicine; the American Association of Physicists in Medicine, the Australasian College of Physical Scientists and Engineers in Medicine, the MICCAI Society, and the Institute of Physics. He has been an executive member of the board of the MICCAI society, as well as its treasurer. He has mentored more than 80 trainees at the Master's, Doctoral and Postdoctoral levels. He was awarded the Erskine Travelling Fellowship by the University of Canterbury in 1996 and again in 2010.

**Lixu GU** (M'04–SM'12) received the Ph.D. degree in computer science from the Toyohashi University of Technology, Toyohashi, Japan, in 1999. Thereafter, he moved to Canada and worked at Robarts Research Institute for 3 years, where he was responsible for the research and software development of the medical image analysis. In 2003, He moved to the Department of Computer Science, Shanghai Jiaotong University, Shanghai, China, where he has set up and directs the laboratory of image guided surgery and therapy (IGST), and appointed as a Professor in the Department of Biomedical Engineering and Med-X Research Institute.

He is the author of over 180 papers on related research area. His research interests include pattern recognition, computer vision, medical image processing, computer graphics, virtual reality, and image guided intervention. He is a social chair and PC member of the 27th IEEE EMBS conference in Shanghai. He was awarded the best poster in the 17th congress of computer assisted radiology and surgery (CARS) in London, U.K., in 2003. He w as an Associate Editor for both the IEEE TRANSACTIONS ON INFORMATION TECHNOLOGY IN BIOMEDICINE and the *International Journal of Computer Assisted Radiology and Surgery*. He is also active in the international research groups of ISBI, MIAR, ITAB, and EMBC.